Bio-Design and Manufacturing (2022) 5:540–555
https://doi.org/10.1007/s42242-022-00191-6

RESEARCH ARTICLE

3D-printed, bi-layer, biomimetic artificial periosteum for boosting bone regeneration

Yage Sun[1] · Ziwei Gao[2] · Xiaoping Zhang[1] · Ziyang Xu[1] · Yahan Zhang[1] · Binbin He[1] · Rong Yang[1] · Qian Zhang[1] · Qiang Yang[2] · Wenguang Liu[1]

Received: 10 December 2021 / Accepted: 13 February 2022 / Published online: 1 April 2022

Abstract

Periosteum, a membrane covering the surface of the bone, plays an essential role in maintaining the function of bone tissue—and especially in providing nourishment and vascularization during the bone regeneration process. Currently, most artificial periostea have relatively weak mechanical strength and a rapid degradation rate, and they lack integrated angiogenesis and osteogenesis functions. In this study, a bi-layer, biomimetic, artificial periosteum composed of a methacrylated gelatin–nano-hydroxyapatite (GelMA-nHA) cambium layer and a poly (N-acryloyl 2-lycine) (PACG) -GelMA-Mg^{2+} fibrous layer was fabricated via 3D printing. The GelMA-nHA layer is shown to undertake the function of improving osteogenic differentiation of rat bone marrow mesenchymal stem cells with the sustainable release of Ca^{2+} from nHA nanoparticles. The hydrogen-bonding-strengthened P(ACG-GelMA-L)-Mg^{2+} hydrogel layer serves to protect the inner defect site and prolong degradation time (60 days) to match new bone regeneration. Furthermore, the released magnesium ion exhibits a prominent effect in regulating the polarization phenotype of macrophage cells into the M2 phenotype and thus promotes the angiogenesis of the human umbilical vein endothelial cells in vitro. This bi-layer artificial periosteum was implanted into a critical-sized cranial bone defect in rats, and the 12-week post-operative outcomes demonstrate optimal new bone regeneration.

Graphic abstract

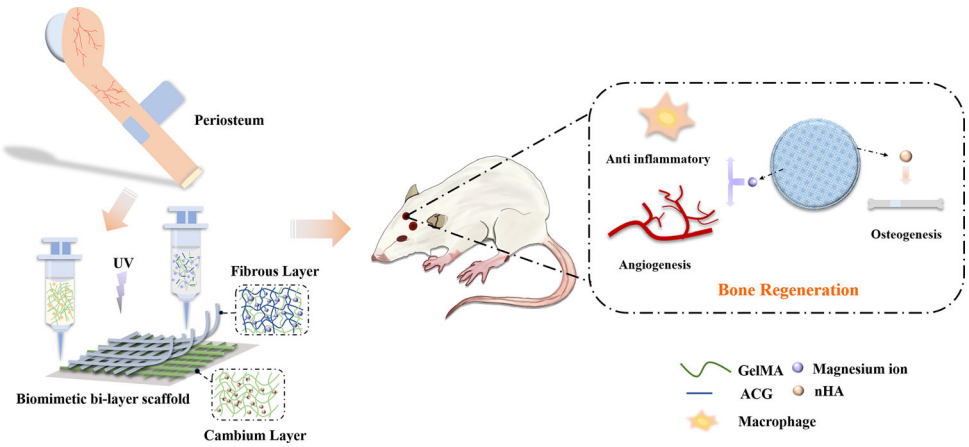

Keywords 3D printing · Bi-layer periosteum scaffold · Immune regulation · Bone regeneration

Yage Sun and Ziwei Gao have contributed equally to this work.

✉ Qiang Yang
yangqiang1980@126.com

✉ Wenguang Liu
wgliu@tju.edu.cn

[1] School of Material Science and Engineering, Tianjin Key Laboratory of Composite and Functional Materials, Tianjin University, Tianjin 300350, China

[2] Department of Spine Surgery, Tianjin Hospital, Tianjin University, Tianjin 300211, China

Introduction

Bone defects caused by trauma, tumors, and genetic diseases have been increasing dramatically in recent years [1, 2]. The therapy of bone defects, especially of critical-size bone defects, still presents a significant challenge to medical personnel. Apart from the gold standards, which are those of autograft and allograft [3, 4], bone tissue engineering has been heralded as an innovative strategy to treat bone defects [5, 6]. In the case of severe bone fracture, the periosteum is also damaged, which is largely ignored in the repair process. Clinical studies have recognized that a damaged periosteum can result in fibrous tissue infiltration into the injured bone, thus hindering repair efficacy [7]. The periosteum is a two-layered membrane covering on the surface of bone [8]. The outer layer is a fibrous layer containing fibroblasts and a nerve and capillary network, which provides nourishment to cells during bone regeneration [9]. The inner layer is cambium with a mass of progenitor cells that can differentiate into osteoblasts and can participate in bone repair once the defect occurs [10]. Thus, the periosteum plays an essential role in maintaining the entire function of bone tissue, especially that of the capillary system and angiogenesis capability. Several studies have focused on the construction of an artificial periosteum to promote the repair of bone defects [11–15]. However, to the best of our knowledge, artificial periostea constructed to date are single-layered, and so, fail to simulate the two-layer microarchitecture of a natural periosteum. In particular, the bioactive function of the fibrous layer is overlooked, adversely affecting ultimate repair efficacy [16, 17]. In addition, the trade-off between the degradation of the artificial periosteum and the rate of new bone growth has not been addressed.

Recently, flourishing three dimensional (3D) printing technology has opened new paths for engineering hierarchal and individualized tissue-engineering scaffolds. To better mimic the microarchitecture of a natural periosteum and eventually boost new bone regeneration, in this study, we designed and fabricated a bi-layered cranial periosteum consisting of cambium and fibrous layer using 3D printing technology. Owing to abundant bioactive sites and better processability [18], methacrylated gelatin (GelMA) was chosen as the major ink. In consideration of the introduction of bone-binding and osteogenic activity, nano-hydroxyapatite (nHA) was added into the GelMA as a co-ink, which is then printed into the biomimetic cambium layer. As the main inorganic component of human and animal bones, nHA can combine with bone tissues through chemical bonds, and the released calcium ions (Ca^{2+}) participate in metabolism in the body to stimulate or induce the regeneration of bones [19–21]. Furthermore, nHA can bind to the polymer chains of GelMA and acts as a reversible crosslink so that toughness and cohesion strength can be enhanced [22–24]. As for the fibrous layer, it takes on the roles of protecting the defective area from outside tissue as well as that of transporting nutrition to the inner cells via the capillary network [25]. To increase the protecting role, a high mechanical strength of the fibrous layer is required [26]. To this end, GelMA and the stimulus-responsive hydrogen-bonding monomer N-acryloyl 2-glycine (ACG) was combined to form a mixture ink, which was customized into a fibrous layer by 3D printing. The GelMA serves to thicken the ink and allows for extrusion-based printing; then the post-polymerization of ACG in the printed objects enhances the mechanical properties of GelMA hydrogel due to the multiple hydrogen-bonding interactions of PACG—something that has been well established in our previous studies [27, 28]. Additionally, the copolymerization of GelMA with ACG can stabilize the transient PACG network with an appropriate in vivo degradation time. To further enhance the repair efficacy of the bone defect, magnesium ions are loaded into the fibrous layer. Magnesium ion has been proven to play a vital role in promoting bone mineralization and angiogenesis [29–32], and in modulating the immune system toward favorable ant-inflammatory pathways [33–36]. Our design concept is depicted in Fig. 1.

Materials and methods

Materials

Glycine (98%, TCI, Shanghai, China), acryloyl chloride (98%, J&K Scientific LTD., Beijing, China), gelatin from porcine skin (type A, reagent grade, Sigma-Aldrich, China), methacrylic anhydride (94%, Heowns Biochemical Technology Company, China), hydroxyapatite (nHA, 96%, Heowns Biochemical Technology Company, China), collagenase (Solarbio Science & Technology Co., Ltd., China), 2-hydroxy-2-methyl-1-phenyl-1-propanone (IRGACURE 1173, 98%, Sigma-Aldrich, St. Louis, USA), $MgCl_2{\cdot}6H_2O$ (98%, aladdin, China), 3-(4,5-Dimethyl-2-thiazolyl)-2,5-diphenyl-2-H- tetrazolium bromide (MTT, 98%, Sigma-Aldrich, China), TRIzol reagent (99%, Sigma-Aldrich, China), and lipopolysaccharide (LPS, 99%, Sigma-Aldrich, China) were used as received from the manufactures. N-acryloyl 2-glycine (ACG), poly(N-acryloyl 2-glycine) hydrogel (termed PACGx—x denotes the initial mass percentage concentration of the ACG monomer), and GelMA were synthesized according to our previous study [24, 25]. All the other chemical reagents were of analytical grade.

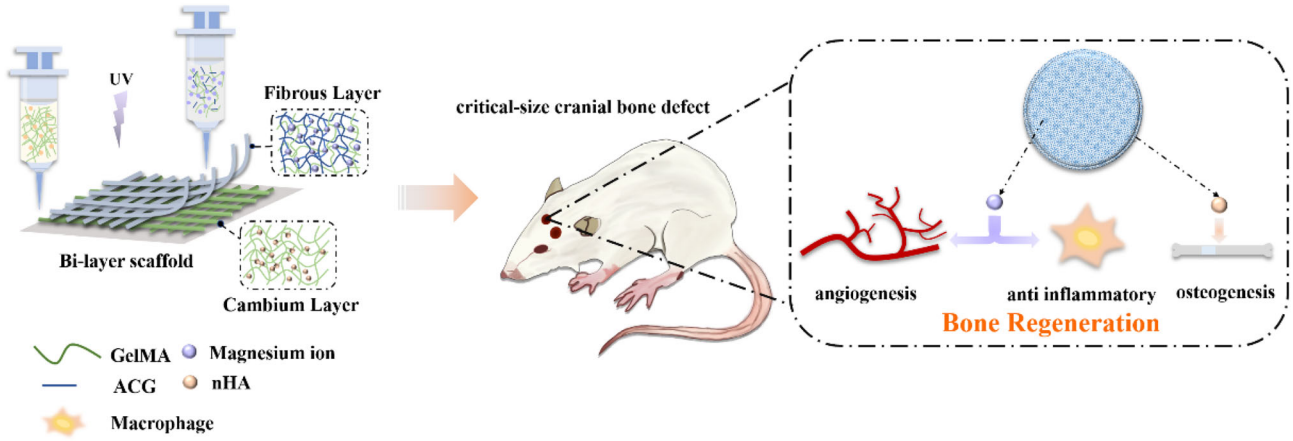

Fig. 1 Schematic illustration of the printing of the bi-layer periosteum scaffold for the repair of a rat's critical-size cranial bone defect

Characterization of GelMA with different degrees of methacrylation (DM)

To determine the DM of the obtained GelMA, gelatin and GelMA were, respectively, dissolved in D_2O. The DM was calculated by the integration of the ^1H NMR spectra. The DM of GelMA can be calculated according to Eq. (1) below [37].

$$\mathrm{DM}\ (\%) = \left(1 - \frac{A\left(\text{lysine methylene of GelMA}\right)}{A\left(\text{lysine methylene of gelatin}\right)}\right) \times 100\%, \quad (1)$$

where A(lysine methylene of gelatin) and A(lysine methylene of GelMA), respectively, represent the integrated areas of lysine methylene at 2.8–2.95 ppm in the spectra of gelatin and GelMA. The resultant GelMAs with a high DM and a low DM are named GelMA-H and GelMA-L, respectively.

Preparation of GelMA-H, GelMA-H-nHA, and P(ACG-GelMA-L)-Mg^{2+} hydrogels

All of the hydrogels were prepared through photoinitiated radical polymerization. Taking the preparation of GelMA-H hydrogel as an example, first, 15 wt% GelMA-H was dissolved in deionized water according to the designed formulations at 40 °C to form a homogeneous solution, into which a 2 wt% photoinitiator IRGACURE 1173 (relative to GelMA) was added. Then, polymerization was conducted in a crosslink oven (XL-1000 UV Crosslinker, Spectronics Corporation, NY, USA) under UV light (365 nm) for 40 min. The acquired hydrogel was named GelMA-H15 (15 represents the initial mass content of the GelMA monomer). Similarly, GelMA and nHA were dispersed homogeneously in deionized water, followed by ultraviolet light (UV light) and illumination for 40 min. Then the GelMA-H15-nHAx hydrogel was obtained, where x denotes a different percent content of nHA (relative to the mass content of GelMA).

For the synthesis of P(ACG-GelMA-L)-Mg^{2+} hydrogels, ACG and GelMA-L were first dissolved in a 20 mM $MgCl_2$ solution, followed by the addition of IRGACURE 1173. In a similar way to the above, P(ACGx-GelMA-Ly)-Mg^{2+} was obtained (x and y denote the mass percent concentration of ACG and GelMA-L, respectively).

Characterizations of hydrogels

Morphological observation of the hydrogels

The surface morphology of the hydrogels was observed through a field-emission scanning electron microscope (FE-SEM, SU1510, Japan) at 5.0 kV. The hydrogels first swelled to equilibrium and lyophilized for 72 h. Then, a gold-coating was applied for 50 s by a sputter coater.

Measurements of dynamic swelling behavior and equilibrium water contents (EWCs) of hydrogels

The dynamic swelling behavior of the hydrogels was tested according to previous work [38]. The swelling ratio (SW) was calculated by the following equation:

$$\mathrm{SW} = \frac{W_t - W_0}{W_0}, \quad (2)$$

where W_t is the wet weight of the swollen hydrogels after immersion in a phosphate buffer saline (PBS) solution for t hours, and W_0 is the initial wet weight of the hydrogel. The experiments were performed in triplicate.

As for the EWCs, the hydrogels were molded into a cylindrical shape and immersed in deionized water for at least 1

week to achieve equilibrium. The wet weight was measured as W_1. Subsequently, the hydrogels were dried completely, and the dry weight was recorded as W_0. The EWCs were calculated using Eq. (3) [39]:

$$\mathrm{EWCs}(\%) = \frac{W_1 - W_0}{W_1} \times 100\%. \tag{3}$$

The experiments were performed in triplicate.

In vitro degradation of hydrogels

Here, we describe the evaluation of the in vitro degradation behaviors of GelMA-H, GelMA-H-nHA, GelMA-L, P(ACG-GelMA-L). 150 mg hydrogels were placed in a centrifuge tube containing 1 mL 5 μg/mL collagenase II solution at 37 °C. The collagenase solution was refreshed every two days. At a specified time-point, all the liquid was sucked out from the centrifuge tube. The remaining hydrogels were lyophilized for 72 h, and then the dry weight at each time-point was recorded as W_t. Specifically, the dry weight of the initial hydrogel was recorded as W_0. The percent residual mass of the hydrogels was calculated according to Eq. (4) [40]:

$$\text{Residual mass } (\%) = W_t / W_0 \times 100\%. \tag{4}$$

The experiments were performed in triplicate.

Analysis of ion release

To evaluate the behavior of the releasing of Ca^{2+} and Mg^{2+} from the hydrogels, an inductive coupled plasma optical emission spectrometer (ICP-MS) was used to determine the amount of released ion. In brief, 200 mg GelMA-H-nHA and 200 mg P(ACG-GelMA-L)-Mg^{2+} hydrogels, respectively, were immersed into a 5 mL PBS solution and were cultivated at 37 °C for 28 days. At a certain time-point, the hydrogels were removed, and the remaining liquid was collected to analyze the ion releasing behavior.

Mechanical properties of the hydrogels

The tests of the mechanical properties of the hydrogels, including tensile strength and compression strength, were conducted on an Instron 2344 Microtester at room temperature. The hydrogels were immersed in the deionized water until equilibrium was reached. Then, the fully swollen hydrogels were punched into dumbbell-shaped samples with a thickness of 0.5 mm for a tensile strength test or molded into cylinder-shaped samples with a diameter of 4.2 mm for a compressive strength test following the reference of the American Society of Testing Materials (ASTM) standard. The stretching rate and cross-head speed setting for the tensile and compression tests were 50 mm/min and 10 mm/min, respectively. The stress of the hydrogel sample was calculated according to Eq. (5):

$$\sigma = \frac{F}{A} \tag{5}$$

where F represents the applied load, and A denotes the initial cross-sectional area.

Rheological measurements of inks

The rheological properties of GelMA-H, GelMA-H-nHA, GelMA-L, and ACG-GelMA-L-Mg^{2+} inks were measured by an Anton Paar MCR302 (Austria) with a 25 mm diameter parallel plate and a gap of 1 mm. The ink was placed on the platform, and the initial temperature was set at 4 °C until gelling was completed. Then, temperature sweep tests were performed over a temperature range from 4 to 40 °C. The heating speed was fixed at 2 °C/min, and the frequency and strain were set at 1 Hz and 0.5%, respectively. In this process, the storage modulus G', the loss modulus G'', and the viscosity were respectively recorded to determine the gel—sol transition point and analyze the trend of change of the viscosity. Then, to verify the shear-thinning properties of the inks, a program was set with the shear rate changing from 0.1 to 1000 s^{-1} at a certain temperature, 27 °C for GelMA-H and GelMA-H-nHAX inks and 18 °C for GelMA-L and ACG-GelMA-L-Mg^{2+} inks, according to the respective condition suitable for printing. Frequency sweeping tests were carried out from 0.005 to 10 Hz at 18 and 27 °C. Further, a program was set with a changing, time-dependent shear rate, and the viscosity was recorded. The time interval was set as 60 s for one step. Also, we examined the self-recovery property in the alternate shear strain test (1%, 100%, 200%, 300%) with a time interval of 60 s, by which the storage modulus G' and the loss modulus G'' were recorded. Finally, taking GelMA-H-nHA ink as an instance, a program was set to simulate the tendency of the variation of viscosity during the printing process.

3D printing of the bi-layer periosteum scaffold

The printing of the bi-layer periosteum scaffold was performed using a 3D extrusion bioprinter (Regenovo, Hangzhou, China). The bi-layer periosteum scaffold was composed of GelMA-H-nHA ink (cambium layer) and ACG-GelMA-L-Mg^{2+} ink (fibrous layer) with a 0.2 mm height for one layer and with eight layers in total. The parameter sets for the two inks were completely different. For the printing of the GelMA-H-nHA ink, prior to loading into the barrel, the inks were pre-heated to 37 °C. The barrel temperature was set at

27 °C, which was near the gel–sol transition point of the ink. During printing, the extrusion speed was fixed at 8 mm/min under a pressure of 0.2 MPa, and the platform temperature was set at 10 °C. For the printing of the ACG-GelMA-L-Mg^{2+} ink, the ink was pre-cooled at 4 °C for at least 20 min to ensure gel formation, and then the ink was transferred into the barrel at 18 °C, according to rheological measurement results. The extrusion speed was set at 10 mm/min under a pressure of 50 kPa. The platform temperature was controlled at − 10 °C to ensure that the printed constructs maintained a gelling state, thus avoiding the collapse of the structure. To obtain a bi-layer periosteum scaffold, different inks loaded into two barrels were alternately printed. Here, four layers of GelMA-H-nHA ink were printed first, and the other four layers of ACG-GelMA-L-Mg^{2+} ink were printed subsequently. Finally, photoinitiated polymerization was performed under UV light for 30 min to ensure the completion of chemical crosslinking.

Assay of cytotoxicity and cell adhesion

The cytotoxicity of the hydrogels was evaluated using an MTT assay with rat bone-marrow mesenchymal stem cells (rBMSCs, Cyagen, China). The GelMA-H-nHA, P(ACG-GelMA-L)-Mg^{2+} hydrogel and bi-layer scaffold were immersed in the culture medium in advance for at least 24 h to obtain the leaching solution. The rBMSCs were seeded in a 96-well plate at a density of 2×10^4 cells per well and incubated for 24 h. Then, the culture medium was removed and refreshed with a 200 μL leaching solution. After culturing for 24 h or 72 h, the medium was replaced with a mixture of the culture medium and MTT (V:V = 9:1) and incubated for an additional 4 h. Finally, all the medium was removed and 200 μL dimethyl sulfoxide (DMSO) was added per well. The absorbance value was measured at 570 nm using a Model 550 microplate reader (Bio-Rad, USA). The non-treated cell was used as a control, and cell viability was calculated with Eq: (6):

$$\text{Cell viability} = I_e/I_c \times 100\%, \tag{6}$$

where I_e and I_c represent the absorbance of the experimental group and control group, respectively.

Cell adhesion tests were conducted through calcein-AM staining. In brief, the GelMA-H-nHA and P(ACG-GelMA-L)-Mg^{2+} hydrogels were placed at the bottom of the 6-well plate. Then, the rBMSCs were seeded on the surface of the hydrogels with a density of 2×10^5 cells per well and cultured for 24 h and 72 h. Afterward, the hydrogels were transferred into a new 6-well plate and stained with calcein-AM. The cells adhesion and proliferation were observed under an inverted fluorescence microscope (EVOS M5000, Invitrogen, China).

Evaluation of in vitro angiogenesis and osteogenesis

To estimate the ability of the magnesium ion to promote angiogenesis, the tube formation experiment was conducted using human umbilical vein endothelial cells (HUVECs). In brief, Matrigel was first coated on the bottom of a 96-plate well, onto which the HUVECs were cultured with a density of 3×10^4. Subsequently, the P(ACG-GelMA-L)-Mg^{2+} hydrogel or bi-layer scaffold was placed into the plate. At a specific time-point (3 h and 6 h), the formed, capillary-like structure was observed under an inverted fluorescence microscope (EVOS M5000, Invitrogen). The numbers of meshes and junctions were analyzed with Image J.

Alkaline phosphatase (ALP) and Alizarin Red S (ARS) staining was performed to assess the osteogenic differentiation of rMSCs. The rMSCs were cultured in 24-well plates at a density of 1×10^5, followed by the addition of GelMA-H, GelMA-H-nHA or bi-layer scaffold. After culturing for 7 days and 14 days, ALP staining was conducted to evaluate the differentiation status in the early stage. ARS staining was used to determine the formation of the mineralized matrix at 14 days and 28 days.

Reverse transcription-polymerase chain reaction (RT-PCR) analysis

First, RT-PCR was conducted to determine whether magnesium ion had the ability to regulate the polarization behavior of macrophages. In brief, RAW246.7 cells were cultured in 6-well plates at a density of 2×10^5 for 24 h, followed by the addition of LPS, treating for 24 h, then P(ACG-GelMA-L) hydrogel, P(ACG-GelMA-L)-Mg^{2+} hydrogel, or a bi-layer scaffold was added, respectively. After culturing for an extra 24 h, the total cellular RNA was extracted by TRIzol (Invitrogen) and reverse transcribed to cDNA. RT-PCR was performed using SYBR Green QPCR Master Mix with a Light Cycler apparatus (Bio-Rad, CFX-Touch). The $2^{-\Delta\Delta CT}$ method was adopted for the quantification of the relative expression of each concerned gene [41]. The sequences of the primers are listed in Table S1 (Supplementary Information). The RNA was extracted from HUVECs and rMSCs. The relative expressions of angiogenesis-related genes (including HIF-1α and VEGF) and osteogenesis-related genes (including ALP, COL-1 and Runx-2) were also measured using RT-PCR.

Assessment of in vivo bone regeneration

All the protocols for animal care and experiments were conducted in accordance with the guidelines of the Council for the Purpose of Control and Supervision of Experiments on Animals, Government of China. The animal experiments were approved by the Animal Ethical Committee of

Orthopedic Research Institute, Tianjin Hospital, Tianjin University (2021 Medical Ethical Review 045). Thirty-nine, male, Sprague–Dawley rats (200–250 g) were randomly divided into three groups: (1) the negative control group (NC, untreated), $n = 13$; (2) the GelMA-H-nHA scaffold group, $n = 13$; and (3) the bi-layer scaffold group, $n = 13$. The rat cranial critical-sized defect model was established following the standard protocol. After general anesthesia, the parietal calvarium was shaved and cleaned. A 3 cm coronal incision was made in the scalp to expose the skull. Then, bilateral, 6 mm, symmetrical, full-thickness cranial defects were constructed using a slow-speed electric trephine drill under continuous irrigation with saline solution. After the defects were filled with scaffolds or left empty as controls, the overlying tissue was closed with an interrupted suture. The rats were sacrificed, and the calvarias were taken out at 8 and 12 weeks post-surgery. The harvested samples were fixed in 4% paraformaldehyde for further investigation. To quantitatively evaluate bone formation within the defects, the specimens were scanned using a micro-CT instrument (GE healthcare, USA) at a resolution of 45 μm. The X-ray settings were standardized to 80 kVp and 450 μA with an exposure time of 400 ms. The 3D images were reconstructed to analyze new bone formation using micro-CT analysis software (Micro View™ ver.2.2). The cylinder region of interest (ROI) was quantified by the values of bone mineral density (BMD), the ratio of bone volume to tissue volume (BV/TV), and trabecular thickness (Tb·Th). After fixation, the isolated specimens were decalcified in EDTA (pH 7.2) for 4 weeks before dehydration and embedding in paraffin. 7 μm-thick histological sections were cut for hematoxylin and eosin staining (H&E), which was captured by fluorescence microscope.

Statistical analysis

The in vitro experiments were analyzed by one-way analysis of variance (ANOVA) with Tukey's post hoc test, and data are expressed as means ± standard deviations (SD). Statistical significance was defined as having $*P < 0.05$. SPSS 20.0 was used for the statistical analysis of data.

Results and discussion

Preparation and characterization of GelMA-H-nHA and P(ACG-GelMA-L)-Mg^{2+} hydrogels

In this present research, which aims to construct a bi-layer biomimetic periosteum with robust mechanical properties and highly efficient bone regeneration ability, we chose the hydrogen-bonding monomer N-acryloyl 2-glycine (ACG) and biocompatible GelMA as the main components of the inks. Here, two kinds of GelMA with different DM were prepared. The integration of ^{1}H NMR spectra was used to calculate the DM (Fig. S1, Supplementary Information). Taking the signal at 6.9–7.5 ppm as a reference and calculating the integration area of lysine methylene at 2.8–2.95 ppm in the spectra of gelatin and GelMA, we obtained one kind of GelMA with a high DM (65.98%) (which we termed GelMA-H) and the other kind of GelMA with a low DM (26.12%) (which we termed GelMA-L). It is necessary to point out that the GelMA-H hydrogel served as a cambium layer due to its robust mechanical property resulted from a higher crosslinking density; while the GelMA-L was used to copolymerize with ACG to form a fibrous layer in view of the stabilizing and strengthening role in the PACG network. To afford osteogenic activity, nHA was dispersed in the GelMA-H aqueous solution, and polymerization was initiated under UV light. We could see that the formed GelMA-H-nHA hydrogel became rough compared with GelMA-H hydrogel on account of an nHA covering on the surface of the hydrogel, as shown in the scanning electron microscope (SEM) images (Fig. S2 in Supplementary Information). Additionally, the XPS spectra in Fig. S2 indicate the presence of Ca and P in the GelMA-H-nHA hydrogel, which verifies the incorporation of nHA in the hydrogel.

An anti-swelling property is critical for the maintenance of the stable mechanical strength of implanted scaffolds in vivo. Fig. S3 (Supplementary Information) shows that the GelMA-H-nHA hydrogels can maintain a stable swelling state in PBS solution, owing to the chemical crosslinking of GelMA and the electrostatic interaction between the polymer chains of GelMA and nHA nanoparticles. Considering the rapid dissociation of the hydrogen-bonding interaction of the PACG network in a neutral medium, ACG was copolymerized with GelMA-L in the presence of Mg^{2+}, which is expected to promote anti-inflammatory properties and angiogenesis. Figure 2a presents the dynamic swelling behavior of P(ACG-GelMA-L)-Mg^{2+} hydrogels with a different content of GelMA-L. It is clear that the pristine PACG hydrogel rapidly swells and ultimately dissolves in PBS within 48 h, while the P(ACG-GelMA-L)-Mg^{2+} hydrogels can keep their integrity and achieve a stable swelling equilibrium within 7 days. This stable swelling originates from both the chemical crosslinking between ACG and GelMA-L and the ion crosslinking between Mg^{2+} and the carboxyl groups of PACG. Notably, with the increasing content of GelMA-L, the SW decreases gradually due to the formation of the denser chemical crosslinking network. The EWCs results shown in Figs. 2b and 2c are consistent with the SW results. Encapsulating nHA barely affects the EWCs of GelMA-H-nHA hydrogels, which are around 85%.

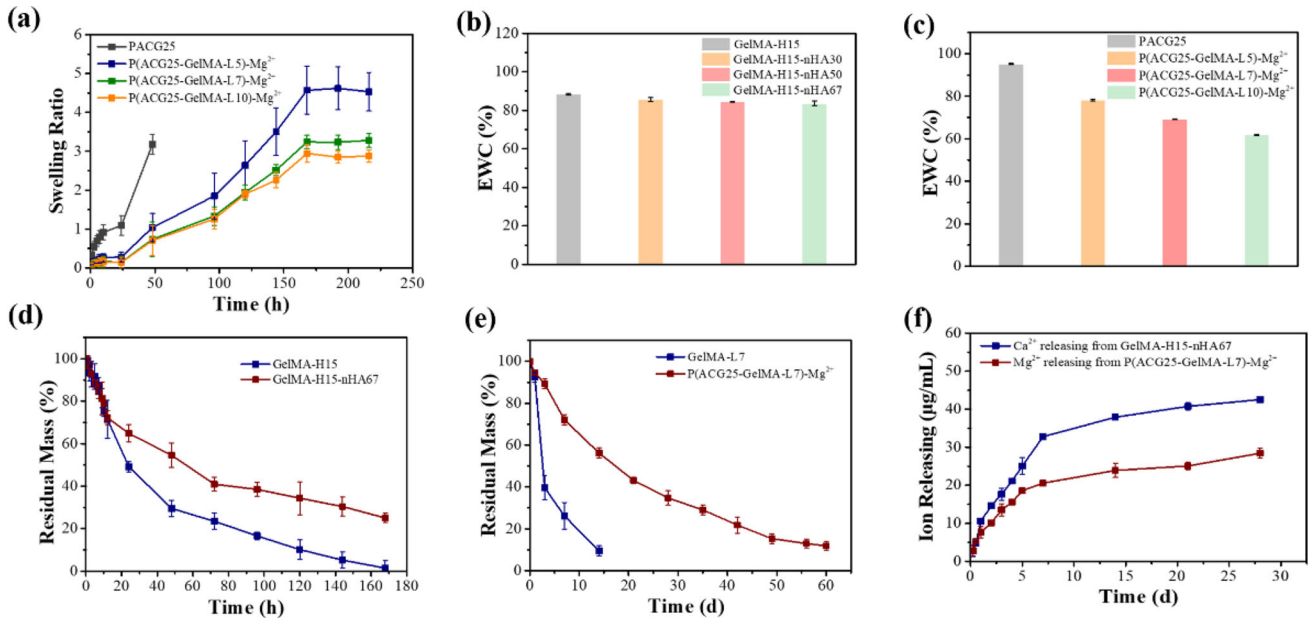

Fig. 2 Physicochemical properties of GelMA-H-nHA hydrogels and P(ACG-GelMA-L)-Mg^{2+} hydrogels: **a** swelling behaviors of PACG and P(ACG-GelMA-L)-Mg^{2+} hydrogels with a different content of GelMA-L; the equilibrium water contents (EWCs) of **b** GelMA-H-nHA hydrogels and **c** P(ACG-GelMA-L)-Mg^{2+} hydrogels; the degradation behaviors of **d** GelMA-H-nHA hydrogels and **e** P(ACG-GelMA-L)-Mg^{2+} hydrogels in PBS with 5 μg/mL collagenase II; **f** dynamic release behaviors of Ca^{2+} and Mg^{2+}

Although the P(ACG-GelMA-L)-Mg^{2+} hydrogels exhibit lower EWCs, they can absorb around 61–78% water.

An appropriate biodegradation rate of a scaffold is vital for the regeneration of new tissue. Figures 2d and 2e exhibit the degradation behaviors of the cast bi-layered hydrogels. As expected, the GelMA-H hydrogel degrades rapidly in collagenase, and almost totally disappears within 168 h. However, the addition of nHA can slow down the degradation rate to a certain degree. Nevertheless, its degradation is still too rapid to match the new bone growth rate. In contrast, the copolymerization of ACG with GelMA-L can significantly inhibit the degradation rate and prolong the degradation time to more than 60 days, which is favorable for bone regeneration. Meanwhile, during the degradation process, Ca^{2+} and Mg^{2+} can be released from the GelMA-H-nHA hydrogel and P(ACG-GelMA-L)-Mg^{2+} hydrogel, respectively, which benefits immune regulation, angiogenesis, and osteogenesis. Figure 2f shows the cumulative releasing behavior of Ca^{2+} and Mg^{2+}. Ca^{2+} is shown to quickly diffuse out in the first 48 h and maintains a slow, sustainable release for about 14 days with the gradual degradation of the GelMA-H-nHA hydrogel. Afterward, Ca^{2+} release does not show significant changes. Similarly, Mg^{2+} demonstrates a continuous releasing behavior from the P(ACG-GelMA-L)-Mg^{2+} hydrogel at a concentration of about 25 μg/mL for the first 14 days, which is cytocompatible [42]. Then, the releasing slows down and lasts for about 28 days. The cumulative releasing ions fall in the range of optimal concentration, which benefits the regulation of macrophage and MSCs' behaviors [43, 44].

We subsequently measured the mechanical properties of the hydrogels. The results are summarized in Figs. 3 and S4. The GelMA-H hydrogel exhibits a relatively low tensile stress with only tens of kPa. Introducing nHA into the GelMA-H leads to a noticeable increase in mechanical strength—the tensile stress and tensile modulus are enhanced to 116.28 kPa and 236.18 kPa, respectively, which are 2.33-fold and 2.4-fold those of the GelMA-H hydrogel when the nHA content is raised to 67%. This mechanical enhancement is considered to stem from interaction of nHA with polymer chains [22], which serves as a physical crosslinking. As for compressive strength, the GelMA-H hydrogel is somewhat brittle with a lower-than-80% compressive strain. Even if the GelMA-H-nHA hydrogel still cannot achieve a satisfactory compressive strain, the brittleness is clearly improved, which is reflected in the increase of compressive stress and the corresponding modulus. In comparison, the copolymerization of ACG with GelMA results in the considerable enhancement of both the tensile stress and the compressive stress of GelMA-L (Fig. S4 in Supplementary Information), due to the multiple H-bonding interactions of PACG [28]. Nevertheless, excessive GelMA leads to a highly dense crosslinking network, adversely affecting the elongation at break accordingly. Taking the comprehensive properties into account, the ACG and GelMA-L contents were fixed at 25% and 7%, respectively. As shown in Figs. 3c and 3d, the P(ACG25-GelMA-L7)-Mg^{2+} hydrogel can withstand a tensile stress of 0.472 MPa and a compressive stress of 2.164 MPa—higher than those of the GelMA hydrogel-based periosteum [24, 45, 46].

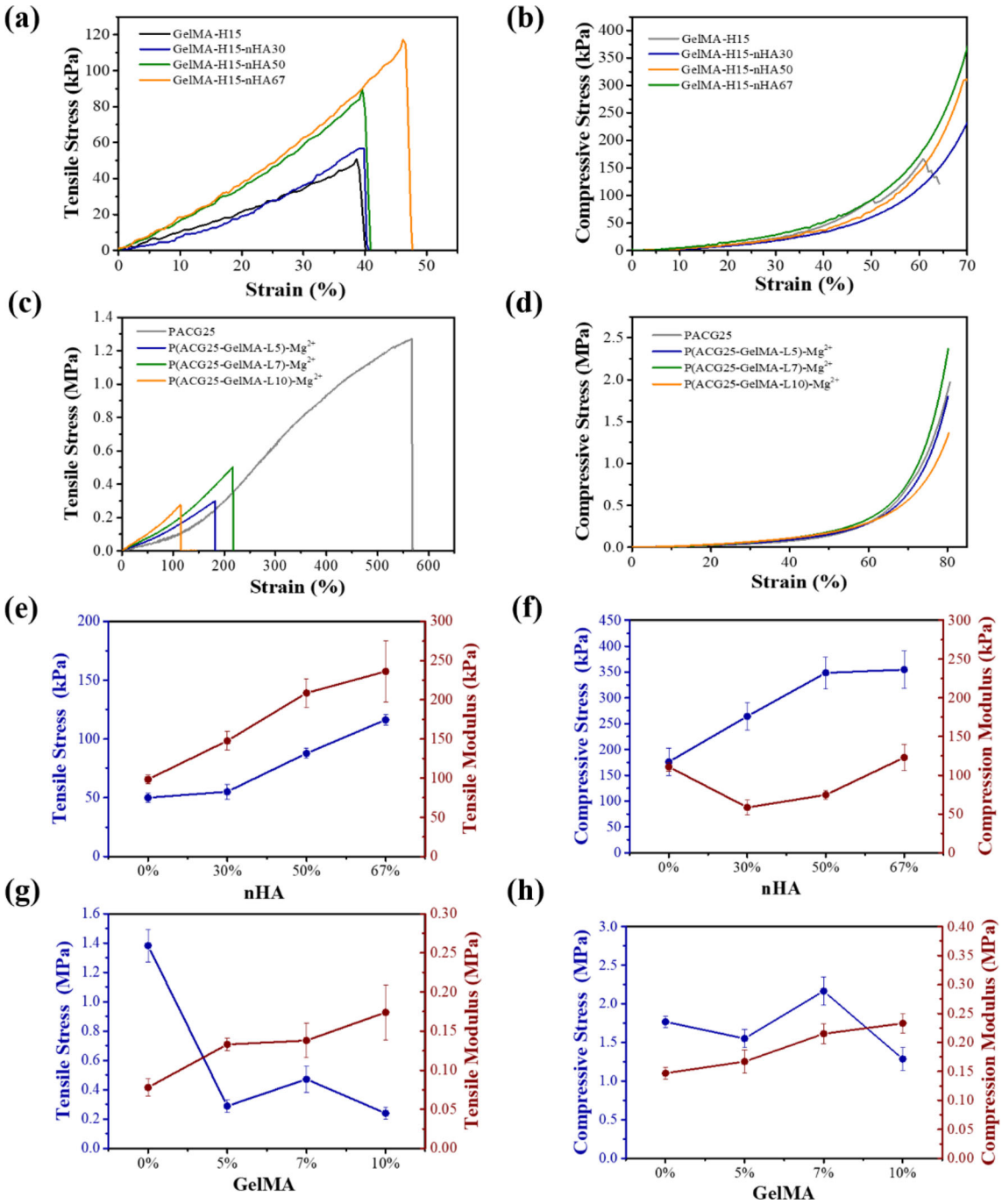

Fig. 3 Mechanical properties of hydrogels: **a** tensile stress and **b** compressive stress of GelMA-H-nHA hydrogels; **c** tensile stress and **d** compressive stress of P(ACG-GelMA-L)-Mg^{2+} hydrogels; **e** tensile stress, tensile modulus, **f** compressive stress, and compressive modulus of GelMA-H-nHA hydrogels with varied nHA content; **g** tensile stress, tensile modulus, **h** compressive stress, and compressive modulus of P(ACG-GelMA-L)-Mg^{2+} hydrogels with a varied GelMA-L content

Rheological properties and 3D printing of the bi-layer scaffolds

A proper initial viscosity, shear-thinning property, and self-supporting property after extrusion are vital characteristics for hydrogel ink to achieve extrusion 3D printability. We next conducted rheological tests to explore the feasibility of the two inks for printing. The temperature sweeping results are shown in Figs. 4a and 4d. The addition of an ACG monomer may disturb the triple-helix structure of GelMA-L, which is manifested by the decrease of gel–sol transition temperature to around 20 °C, while the addition of an nHA to GelMA-H aqueous solution does not bring about an apparent change to the gel–sol transition temperature, which

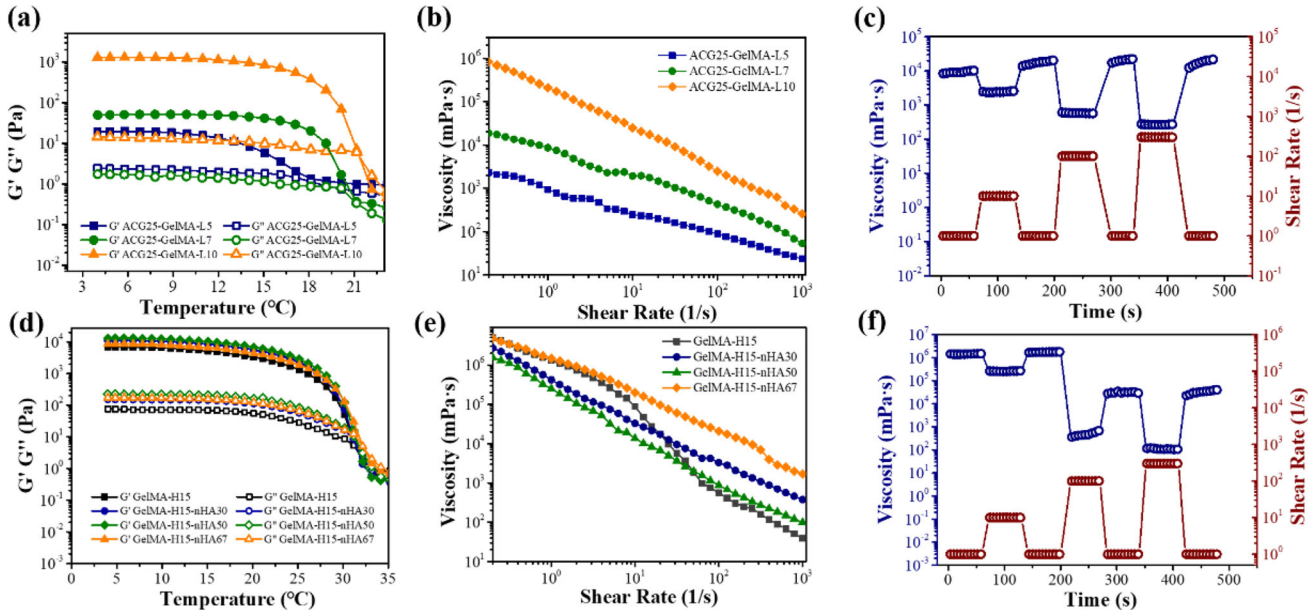

Fig. 4 Rheological measurements of two bioinks: **a** and **d**—temperature sweeping of ACG-GelMA-L and GelMA-H-nHA ink; **b** and **e**—shear-thinning properties of ACG-GelMA-L and GelMA-H-nHA ink; **c** and **f**—the cyclic sweeping of the shear rate (1, 10, 100, 1000 1/s) for two inks

is around 31 °C. Figures 4b and 4e present the shear-thinning curve of the inks. Notably, both the ACG-GelMA-L-Mg^{2+} and GelMA-H-nHA inks have initial viscosities suitable for 3D printing [47]. With an increasing shear rate, the viscosity of the inks decreases continuously, showing a typical shear-thinning characteristic. The alternate step strain sweeps in Figs. 4c and 4f reveal that the viscosity of the inks is able to respond instantly to the shear force, further confirming the shear-thinning property of the inks. As shown in Fig. S6 (Supplementary Information), when the temperature is below the gel–sol transition point, the inks retain the gelling state and the viscosity is nearly constant. As the temperature approaches the gel–sol transition point, the viscosity decreases due to a breakup of hydrogen-bonding interaction in the network. From the viscosity-temperature curves, the ultimate extrusion temperatures are determined to be 27 °C and 18 °C for GelMA-H-nHA ink and ACG-GelMA-L-Mg^{2+} ink, respectively. Frequency sweeping tests were subsequently carried out at 27 °C and 18 °C, and the results indicate that the inks keep a stable modulus over a broad range of frequencies. Additionally, the curves of the alternate shear strain sweeping present a rapid recovery of the modulus. At a low shear strain (1%), the G' and G'' keep nearly constant, and G' is dominant over G'', suggesting a gelling state due to hydrogen-bond interactions. Upon increasing the shear strain to 100%, 200%, and 300%, G' and G'' gradually come closer to each other, and eventually a gel–sol transition occurs at a high shear strain (300%). Once the shear strain falls back to 1%, G' and G'' can recover to their initial state in less than 30 s, which verifies the rapid reconstruction of the hydrogen bonds. The above results of the rheological tests indicate that the GelMA-H-nHA and ACG-GelMA-L-Mg^{2+} inks are suitable for extrusion 3D printing.

In light of their mechanical and rheological properties, the GelMA-H15-nHA67 and ACG25-GelMA-L7-Mg^{2+} inks were selected for the following experiments. Figure 5a shows the changes of viscosity of GelMA-H15-nHA67 ink by simulating the simultaneous variation of temperature and shear rate during printing. Specifically, the ink is pre-cooled to 4 °C, so that the viscosity keeps a relatively high value in the gel state. When the ink is transferred into the barrel and the temperature is increased to 27 °C, the viscosity of the ink decreases slightly at a low shear rate. Then, the viscosity obviously decreases with the increase of the shear rate during extrusion printing at 27 °C. Eventually, the ink recovers to the initial state after being extruded on the cryogenic platform and can retain a stable status until the photoinitiated polymerization occurs. Figures 5b and 5c show the printed multi-layer grid structures of the GelMA-H15-nHA67 and ACG25-GelMA-L7-Mg^{2+} ink, respectively. The filaments remain stable after extrusion, and almost no collapse occurs in the structures, owing to the self-supporting ability of the inks. The clear gridding structure formed by the filaments can be observed in Fig. 5d, confirming that the printed construct retains a high fidelity. The high resolution and stability of the construct can be attributed to the favorable rheological properties of the inks. The bi-layer biomimetic periosteum scaffold is constructed through the alternate printing of the two inks. Specifically, four layers of GelMA-H15-nHA67 ink are first printed to mimic the cambium layer, onto which then three layers of ACG25-GelMA-L7-Mg^{2+} ink are printed to fabricate the fibrous layer. To match the size of the bone

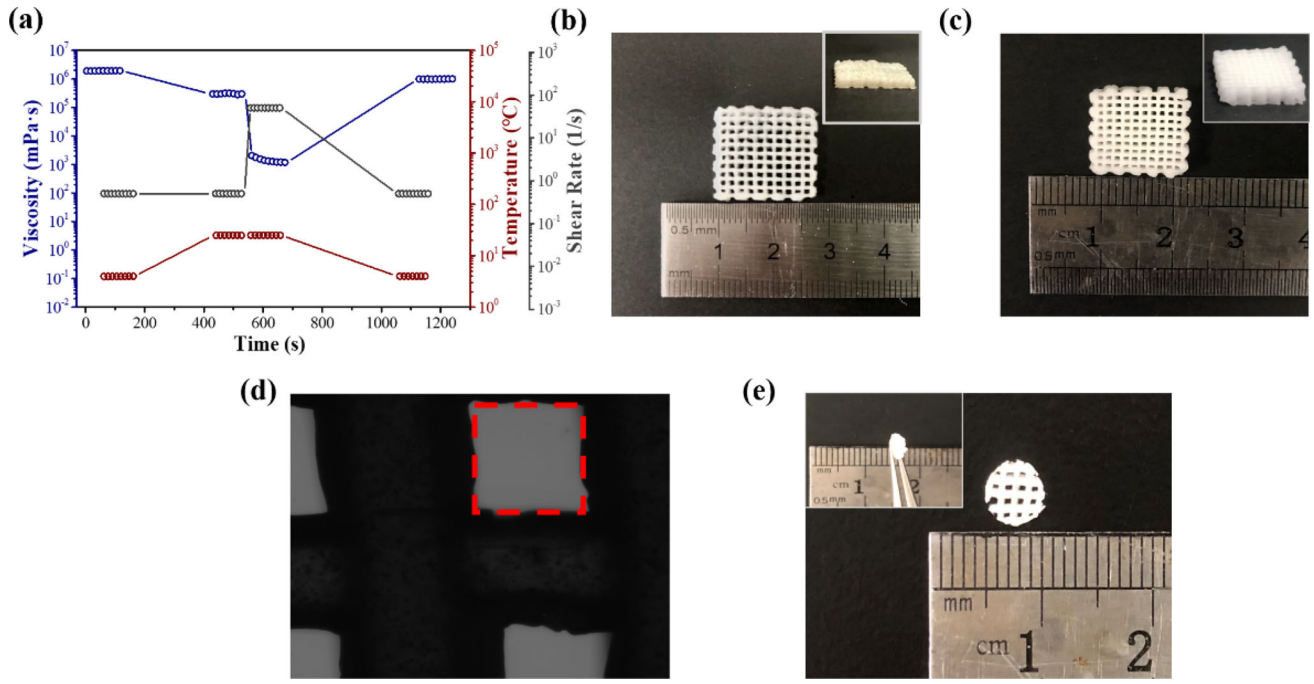

Fig. 5 The mimicking 3D printing process and images of the printed structures: **a** the simulated extrusion process of GelMA-H-nHA ink during 3D printing with the variation of viscosity in response to the simultaneous change of temperature and shear rate; **b** a digital photo of the printed GelMA-H-nHA grids with a thickness of 2 mm; **c** a digital photo of the printed ACG-GelMA-L-Mg^{2+} grids with a thickness of 2 mm; **d** a local, magnified photo of **C** with a high fidelity; **e** a digital photo of the bi-layer periosteum scaffold with a diameter of 6 mm and a thickness of 1 mm

defect model in vivo, a periosteum scaffold with a diameter of 6 mm and thickness of 1 mm is printed (Fig. 5e).

In vitro biological evaluation of the scaffolds

Biocompatibility is an essential requirement for a biomaterial that is promising for development as a tissue-engineering scaffold. So, the cytotoxicity and cell affinity of P(ACG25-GelMA-L7)-Mg^{2+} hydrogel and GelMA-H-nHA hydrogel were examined in this research. Figure 6a shows the cell viability of rBMSCs after cultivation in the leaching solution of the hydrogels for 24 h and 72 h. The results indicate that both layers have better biocompatibility with over 95% cell viability in 24 h, because the components in the system are all biologically benign and the magnesium ion concentration is limited to the safe range, which is 20 mM, according to previous work [33]. Even after cultivating for 72 h, the cells remain highly viable. Figure 6b presents the results of cell adhesion on the two layers of the scaffold using calcein staining. It is clear that the rBMSCs can effectively spread out on the scaffolds with spindle shapes. Prolonging the culture time to 72 h, more cells can be observed and nearly cover the whole surface of the scaffold. This means that the cells can not only adhere on the scaffold but also maintain high proliferation. The benign cell affinitive ability is ascribed to the introduction of GelMA, whose RGD sequence has been recognized for promoting cell adhesion and proliferation [48, 49].

In vitro immune regulation and angiogenesis function of magnesium ion

The early stage of the inflammatory reaction of immune cells and angiogenesis have been recognized to play a critical role in bone tissue regeneration [42, 50]. In consideration of immune regulation and angiogenesis functions, magnesium ion was introduced into the bi-layer scaffold system and can be released at an appropriate range of concentration through the hydrogel network. The modulation of immune responses of magnesium ion was assayed by RT-PCR. Figures 7a–7d show that all the macrophage cells express high levels of pro-inflammatory cytokines (TNF-α, iNOS, IL-6, IL-1β) under the stimulation of LPS. The hydrogels without magnesium ions show negligible modulation effects. This is embodied in the high expression levels of pro-inflammatory cytokines. In comparison, with the addition of magnesium ion, the expression levels of pro-inflammatory cytokines decrease considerably in both P(ACG-GelMA-L)-Mg^{2+} hydrogel and the bi-layer scaffold. This result suggests that the magnesium ion releasing from the hydrogel network can effectively downregulate the expression of pro-inflammatory cytokines via inhibiting the activation of NF-kB and TLR pathways and

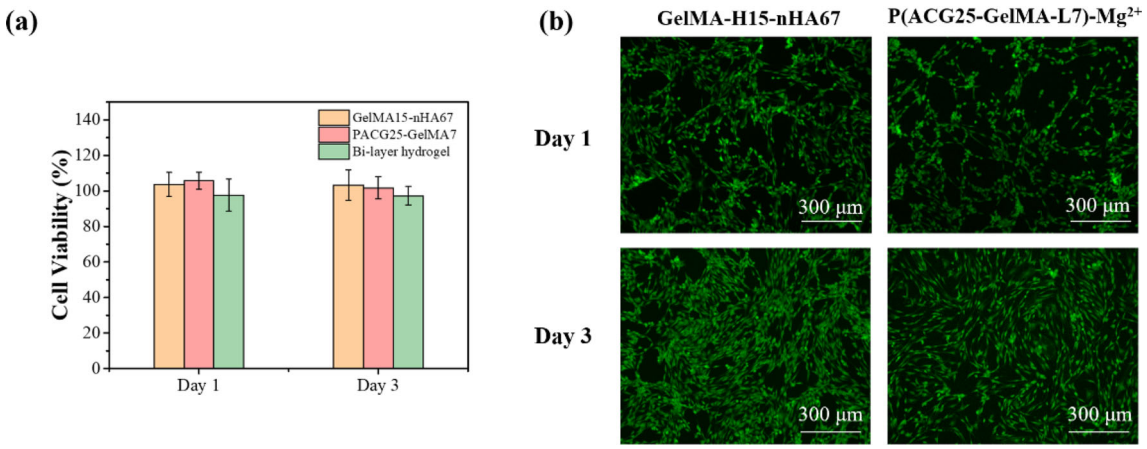

Fig. 6 In vitro biological evaluation of the scaffolds: **a** cell viability of the GelMA-H15-nHA67 hydrogel, the P(ACG25-GelMA-L7)-Mg^{2+} hydrogel, and bi-layer scaffold detected at 24 h and 72 h; **b** rMSCs adhesion on the GelMA-H15-nHA67 hydrogel and P(ACG25-GelMA-L7)-Mg^{2+} hydrogel detected at 24 h and 72 h

thus reduce the M1 phenotype polarization of macrophage cells [33].

Subsequently, the ability of magnesium ions to promote angiogenesis was assessed by tube formation experiments. Images of the capillary-like network formed by HUVECs under the stimulation of different hydrogels are shown in Fig. 7e, and an analysis of the numbers of meshes and junctions is shown in Figs. 7f and 7g. As shown in the figures, the addition of magnesium ion facilitates the formation of the capillary network in 3 h when compared with the negative control (NC) group. Further prolonging the culture time to 6 h, minor tubes are formed in the NC group, while both the P(ACG-GelMA-L)-Mg^{2+} hydrogel and the bi-layer significantly enhance the number of meshes and junctions, implying their potent pro-angiogenesis ability. Moreover, the bi-layer scaffold demonstrates a stronger effect on the formation of the capillary network due to the synergy of magnesium ion and nHA nanoparticles, which has been reported to have the function of promoting angiogenesis [51]. To better illustrate the effect of magnesium ion on angiogenesis, the expression of mRNA, including VEGF and HIF-1α, is assessed through RT-PCR (Figs. 7h and 7i). It is evident that the expression levels of VEGF and HIF-1α are significantly increased with the addition of magnesium ion compared with the NC group. This is consistent with the results of the tube formation experiments. Thus, we can assume that magnesium ion promotes angiogenesis via the upregulation of the expression of VEGF and HIF-1α, which is also beneficial for osteogenesis.

Assessment of in vitro osteogenesis

We next inspected the effect of different hydrogels on the osteogenic differentiation ability of rMSCs. The best-visualized method is with ALP and ARS staining, as presented in Fig. 8a. ALP is a critical component of bone-matrix vesicles. It plays an essential role in the initial stages of bone-matrix mineralization and is deemed to be an early indicator of osteoblastic metabolic activity [52]. Purple ALP staining can be weakly seen on day 3, while stronger staining can be observed on day 7. Moreover, the combined addition of nHA and magnesium ion results in a much higher ALP expression level, which is reflected in the larger and denser staining area. As a marker of calcium mineral deposition in the late stage of osteogenesis, ARS staining was performed on day 14 and day 28 post-operation. The bi-layer scaffold group shows a stronger matrix mineralization level compared with the other three groups, corroborating its higher potential in promoting bone regeneration. The results of staining are reconfirmed via the results of RT-PCR (Figs. 8b–8d), in which the relative expression levels of the osteogenic marker genes—including Runx-2, ALP, and COL-1—are detected. Consistently with the ALP and ARS staining results, the expression levels of these genes are remarkably upregulated under the stimulation of the bi-layer scaffold. Hence, the bi-layer scaffold shows promise to be developed as an artificial periosteum for promoting bone regeneration.

Assessment of in vivo bone regeneration

To evaluate the bone repair effect of the 3D-printed bi-layer scaffold, a 6 mm critical-sized cranial bone defect rat model was established in this experiment. The negative control (NC) group and GelMA-H-nHA group were set as a comparison. The bone repair and regeneration effect was observed and analyzed by microcomputed tomography (Micro-CT), and the results are presented in Fig. 9. As shown in Fig. 9a, calcified bone tissues had already appeared in the three groups by 8 weeks, while the density and volume of the bone formation show a remarkable difference. Clearly, the bi-layer scaffold demonstrates the

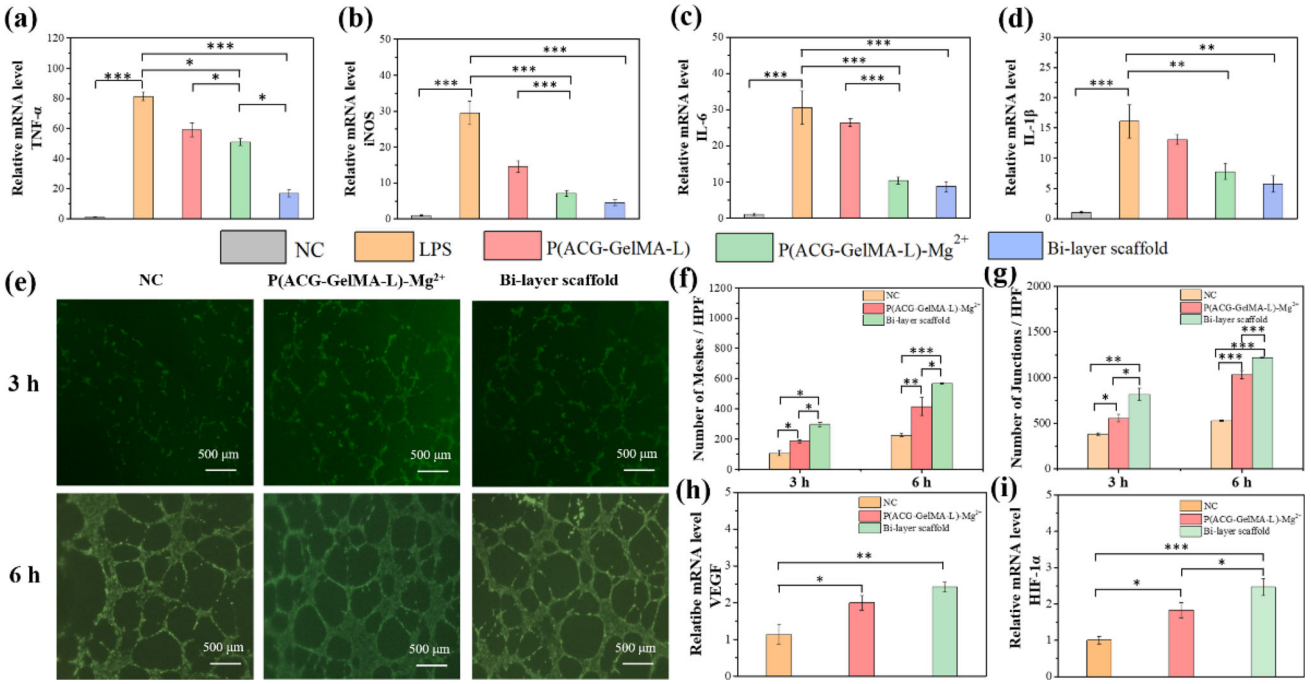

Fig. 7 In vitro immune regulation and angiogenesis function of magnesium ion: **a**–**d** relative expression levels of pro-inflammatory cytokines (TNF-α, iNOS, IL-6, IL-1β), *NC* negative control; **e** images of the capillary-like network formed by HUVECs at 3 h and 6 h; **f** analysis of the number of meshes formed in the capillary network, *NC* negative control; **g** analysis of the number of junctions formed in the capillary network, *NC* negative control; **h**, **i** expression levels of angiogenesis-related mRNA (VEGF and HIF-1α), *NC* negative control; $^{*}P < 0.05$, $^{**}P < 0.01$, $^{***}P < 0.001$

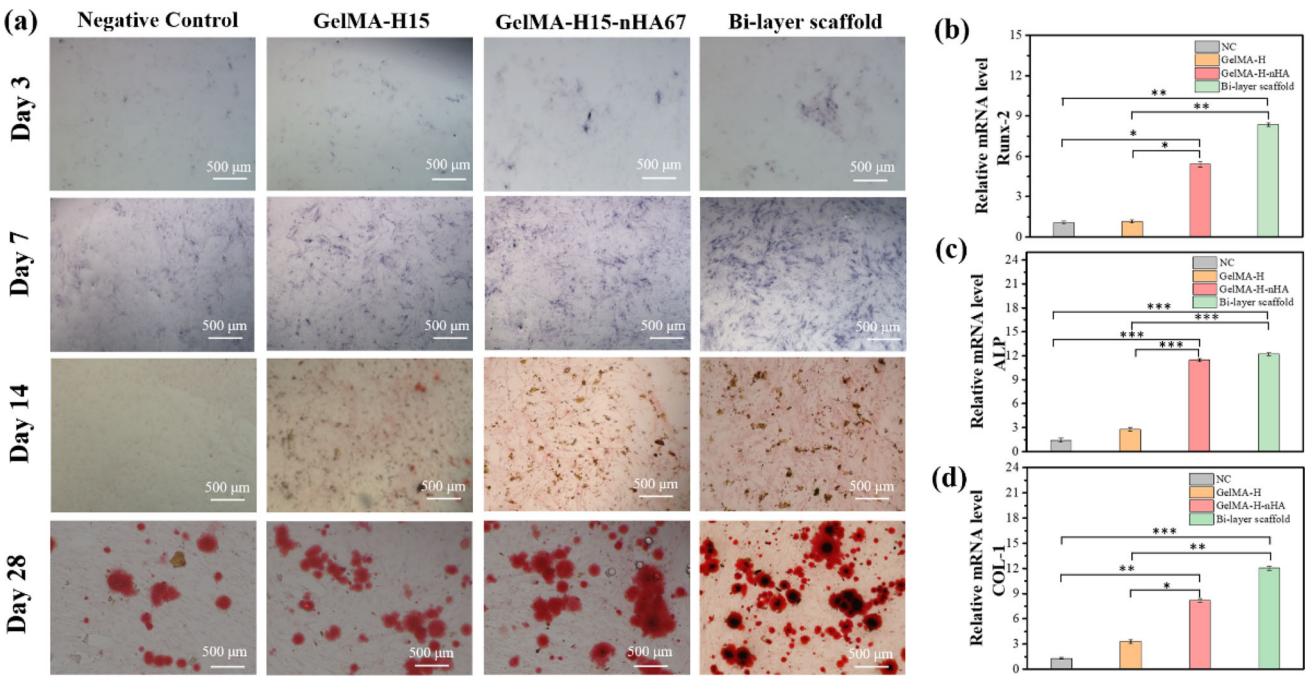

Fig. 8 Assessment of in vitro osteogenesis: **a** ALP and ARS staining of rMSCs to assess osteogenic differentiation; **b**–**d** relative expression levels of osteogenic marker genes of Runx-2, ALP, and COL-1, *NC* negative control; $^{*}P < 0.05$, $^{**}P < 0.01$, $^{***}P < 0.001$

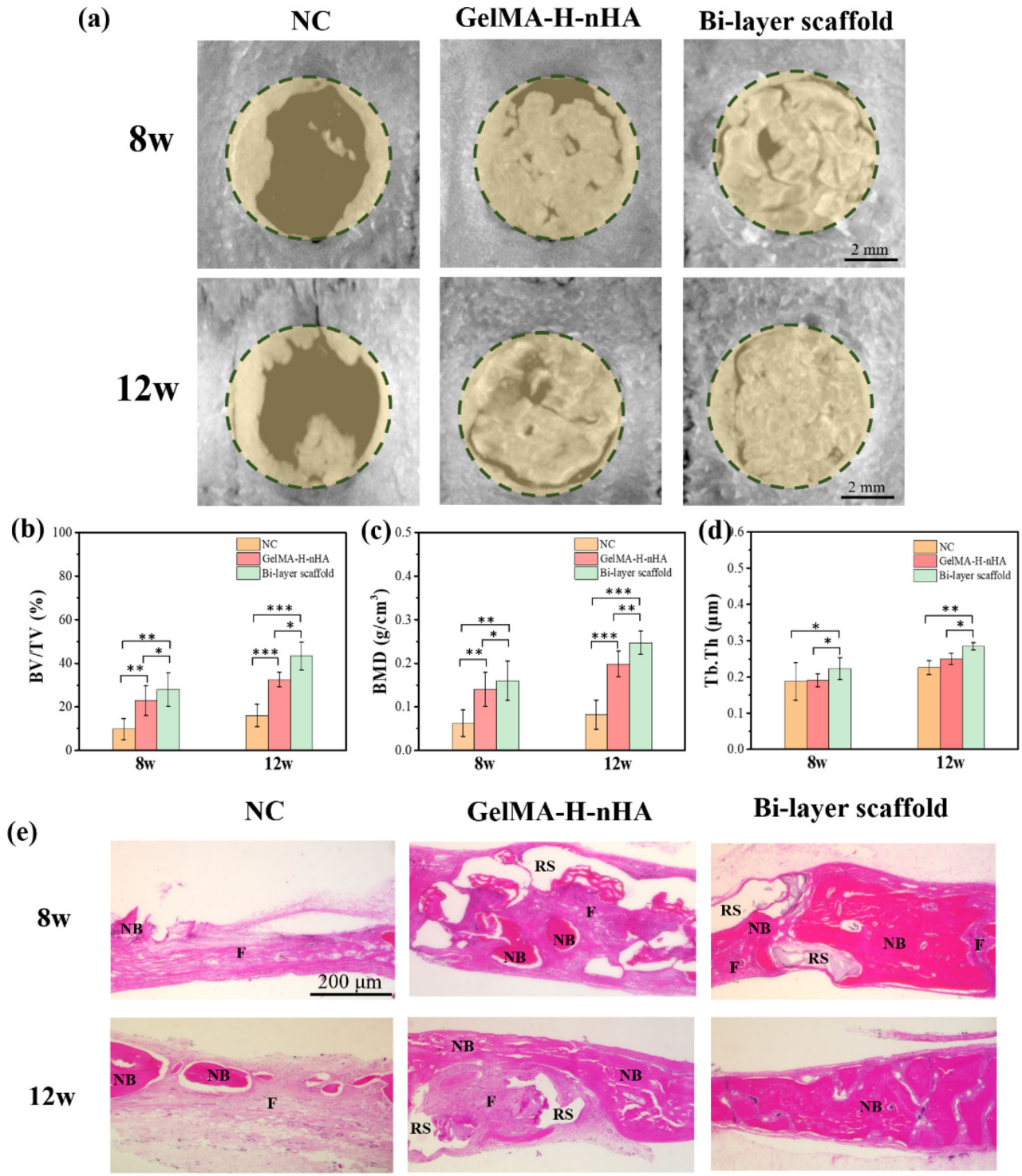

Fig. 9 Assessment of in vivo bone regeneration: **a** micro-CT images of bone defect areas after implantation for 8 weeks and 12 weeks; **b**–**d** quantitative analysis of BV/TV, BMD, and Tb.Th of the new bone tissue at 8 weeks and 12 weeks; **e** HE staining of cranial bone defect areas at 8 weeks and 12 weeks post-implantation (4x)—NB, F, and RS represent new bone tissue, fibrous tissue, and residual scaffolds, respectively; $^{*}P < 0.05$, $^{**}P < 0.01$, $^{***}P < 0.001$

highest repairing efficiency due to the synergetic effect of the biomimetic cambium layer and fibrous layer, as noted above. Furthermore, when prolonging the observation time to 12 weeks, the newly formed bone tissue is increased even more, and the bi-layer scaffold still has an advantageous repair effect. The micro-CT results are highly consistent with the analysis results of bone tissue volume/total tissue volume (BV/TV) and bone mineral density (BMD) (Figs. 9b and 9c). Additionally, with the maturation of the forming bone tissue, the trabecular thickness (Tb.Th) in the new bone area increases significantly, as shown in Fig. 9d. The osteogenic function of the scaffolds was also verified through HE staining (Fig. 9e), in which the specimen treated with the bi-layer scaffold exhibits the highest osteogenic activity, and the specimens in NC group and GelMA-H-nHA scaffold group show more areas of fibrous tissue. The results of the HE staining are consistent with those of the micro-CT. Thus, under the concerted action of magnesium ion and nHA nanoparticles, the 3D-printed bi-layer scaffold contributes to an optimal therapy for treatment of critical-sized bone defects.

Conclusions

In this study, we successfully fabricated a bi-layer, biomimetic artificial periosteum via 3D printing. GelMA and nHA nanoparticles were printed into a cambium layer. The formed GelMA-H-nHA hydrogel possessed appropriate mechanical properties and rapid degradation behavior. Calcium ions could be released from nHA nanoparticles at a suitable rate during the degradation process of the hydrogels, and the released Ca^{2+} facilitated the osteogenesis differentiation of rMSCs. To better restore the function of the outer fibrous layer with a capillary network that provides nourishment to the cells during the bone regeneration process, the P(ACG-GelMA-L)-Mg^{2+} hydrogel was printed on the surface of the GelMA-H-nHA hydrogel cambium layer. The robust mechanical properties and long degradation time (up to over 60 days) of the P(ACG-GelMA-L)-Mg^{2+} hydrogel could remedy the weakness of the inner cambium layer, thus preventing the outer tissue from infiltrating into the defect site and making the degradation rate of scaffold match the new bone regeneration. In addition, the magnesium ions releasing from the hydrogel fell into the proper concentration that was effective for regulating the polarization phenotype of macrophage cells into the M2 phenotype and promoting the angiogenesis of HUVECs. Integrating immune regulation, angiogenesis, and osteogenesis functions, this bi-layer biomimetic artificial periosteum contributed to highly efficient bone regeneration in critical-size bone defects in rats.

Supplementary Information The online version contains supplementary material available at https://doi.org/10.1007/s42242-022-00191-6.

Acknowledgements The authors gratefully acknowledge the support for this work from the National Key Research and Development Program (No. 2018YFA0703100) and the National Natural Science Foundation of China (No. 51733006).

Author contributions YS: conceptualization, methodology, formal analysis, investigation, writing—original draft. ZG: resources, investigation. XZ: investigation, resources, visualization, methodology. ZX: formal analysis, methodology. YZ: methodology, resources. BH: methodology, resources. RY: investigation, resources, visualization. QZ: resources, visualization, methodology. QY: funding acquisition, methodology, resources. WL: conceptualization, methodology, writing—review & editing, supervision, project administration, funding acquisition, resources.

Declarations

Conflict of interest The authors declare that they have no conflict of interest.

Ethical approval The animal experiments in this work have obtained the permission from Tianjin Hospital Animal Experimental Ethics Committee.

References

1. Vallet-Regi M, Ruiz-Hernandez E (2011) Bioceramics: from bone regeneration to cancer nanomedicine. Adv Mater 23(44):5177–5218. https://doi.org/10.1002/adma.201101586
2. Habibovic P, Barralet JE (2011) Bioinorganics and biomaterials: bone repair. Acta Biomater 7(8):3013–3026. https://doi.org/10.1016/j.actbio.2011.03.027
3. Wieding J, Lindner T, Bergschmidt P et al (2015) Biomechanical stability of novel mechanically adapted open-porous titanium scaffolds in metatarsal bone defects of sheep. Biomaterials 46:35–47. https://doi.org/10.1016/j.biomaterials.2014.12.010
4. Zhang M, Matinlinna JP, Tsoi JKH et al (2020) Recent developments in biomaterials for long-bone segmental defect reconstruction: a narrative overview. J Orthop Translat 22:26–33. https://doi.org/10.1016/j.jot.2019.09.005
5. Guglielmotti MB, Olmedo DG, Cabrini RL (2019) Research on implants and osseointegration. Periodontol 2000 79(1):178–189. https://doi.org/10.1111/prd.12254
6. Yu W, Li R, Long J et al (2019) Use of a three-dimensional printed polylactide-coglycolide/tricalcium phosphate composite scaffold incorporating magnesium powder to enhance bone defect repair in rabbits. J Orthop Transl 16:62–70. https://doi.org/10.1016/j.jot.2018.07.007
7. Urban IA, Monje A (2019) Guided bone regeneration in alveolar bone reconstruction. Oral Maxillofac Surg Clin North Am 31(2):331–338. https://doi.org/10.1016/j.coms.2019.01.003
8. Baldwin JG, Wagner F, Martine LC et al (2017) Periosteum tissue engineering in an orthotopic in vivo platform. Biomaterials 121:193–204. https://doi.org/10.1016/j.biomaterials.2016.11.016
9. Shi X, Fujie T, Saito A et al (2014) Periosteum-mimetic structures made from freestanding microgrooved nanosheets. Adv Mater 26(20):3290–3296. https://doi.org/10.1002/adma.201305804

10. Allen MR, Hock JM, Burr DB (2004) Periosteum: biology, regulation, and response to osteoporosis therapies. Bone 35(5):1003–1012. https://doi.org/10.1016/j.bone.2004.07.014
11. Wu M, Han Z, Liu W et al (2021) Silk-based hybrid microfibrous mats as guided bone regeneration membranes. J Mater Chem B 9(8):2025–2032. https://doi.org/10.1039/d0tb02687e
12. Lu Z, Wang W, Zhang J et al (2020) Electrospun highly porous poly(L-lactic acid)-dopamine-SiO_2 fibrous membrane for bone regeneration. Mater Sci Eng C Mater Biol Appl 117:111359. https://doi.org/10.1016/j.msec.2020.111359
13. Li B, Chen Y, He J et al (2020) Biomimetic membranes of methacrylated gelatin/nanohydroxyapatite/poly(L-lactic acid) for enhanced bone regeneration. Acs Biomater Sci Eng 6(12):6737–6747. https://doi.org/10.1021/acsbiomaterials.0c00972
14. Yang YH, Xu TP, Bei HP et al (2021) Sculpting bio-inspired surface textures: an adhesive janus periosteum. Adv Funct Mater 31(37):210463610. https://doi.org/10.1002/adfm.202104636
15. Xing JQ, Peng X, Li AQ et al (2021) Gellan gum/alginate-based ca-enriched acellular bilayer hydrogel with robust interface bonding for effective osteochondral repair. Carbohydr Polym 270:118382. https://doi.org/10.1016/j.carbpol.2021.118382
16. Wu L, Gu Y, Liu L et al (2020) Hierarchical micro/nanofibrous membranes of sustained releasing vegf for periosteal regeneration. Biomaterials 227:119555. https://doi.org/10.1016/j.biomaterials.2019.119555
17. Xin T, Gu Y, Cheng R et al (2017) Inorganic strengthened hydrogel membrane as regenerative periosteum. ACS Appl Mater Interfaces 9(47):41168–41180. https://doi.org/10.1021/acsami.7b13167
18. Malafaya PB, Silva GA, Reis RL (2007) Natural-origin polymers as carriers and scaffolds for biomolecules and cell delivery in tissue engineering applications. Adv Drug Deliv Rev 59(4–5):207–233. https://doi.org/10.1016/j.addr.2007.03.012
19. Yang J, Zhang YS, Yue K et al (2017) Cell-laden hydrogels for osteochondral and cartilage tissue engineering. Acta Biomater 57:1–25. https://doi.org/10.1016/j.actbio.2017.01.036
20. Liang XY, Duan PG, Gao JM et al (2018) Bilayered plga/plga-hap composite scaffold for osteochondral tissue engineering and tissue regeneration. ACS Biomater Sci Eng 4(10):3506–3521. https://doi.org/10.1021/acsbiomaterials.8b00552
21. Cai LJ, Xu DY, Chen HX et al (2021) Designing bioactive micro-/nanomotors for engineered regeneration. Eng Regener 2:109–115. https://doi.org/10.1016/j.engreg.2021.09.003
22. Cui CY, Wu TL, Gao F et al (2018) An autolytic high strength instant adhesive hydrogel for emergency self-rescue. Adv Funct Mater 28(42):1804925. https://doi.org/10.1002/adfm.201804925
23. Meredith HJ, Jenkins CL, Wilker JJ (2014) Enhancing the adhesion of a biomimetic polymer yieldsperformance rivaling commercial glues. Adv Funct Mater 24(21):3259–3267. https://doi.org/10.1002/adfm.201303536
24. Nicolay R, Kamada J, Van Wassen A et al (2010) Responsive gels based on a dynamic covalent trithiocarbonate cross-linker. Macromolecules 43(9):4355–4361. https://doi.org/10.1021/ma100378r
25. Zhang X, Awad HA, O'keefe RJ et al (2008) A perspective: engineering periosteum for structural bone graft healing. Clin Orthop Relat Res 466(8):1777–1787. https://doi.org/10.1007/s11999-008-0312-6
26. Yang Y, Xu T, Zhang Q et al (2021) Biomimetic, stiff, and adhesive periosteum with osteogenic-angiogenic coupling effect for bone regeneration. Small 17(14):e2006598. https://doi.org/10.1002/smll.202006598
27. Gao F, Zhang Y, Li Y et al (2016) Sea cucumber-inspired autolytic hydrogels exhibiting tunable high mechanical performances, repairability, and reusability. ACS Appl Mater Interfaces 8(14):8956–8966. https://doi.org/10.1021/acsami.6b00912
28. Gao F, Xu Z, Liang Q et al (2019) Osteochondral regeneration with 3D-printed biodegradable high-strength supramolecular polymer reinforced-gelatin hydrogel scaffolds. Adv Sci 6(15):1900867. https://doi.org/10.1002/advs.201900867
29. Yu Y, Jin G, Xue Y et al (2017) Multifunctions of dual zn/mg ion co-implanted titanium on osteogenesis, angiogenesis and bacteria inhibition for dental implants. Acta Biomater 49:590–603. https://doi.org/10.1016/j.actbio.2016.11.067
30. Wei Y, Shi MS, Zhang JL et al (2020) Autologous versatile vesicles-incorporated biomimetic extracellular matrix induces biomineralization. Adv Funct Mater 30(21):2000015. https://doi.org/10.1002/adfm.202000015
31. Zhang X, Huang P, Jiang G et al (2021) A novel magnesium ion-incorporating dual-crosslinked hydrogel to improve bone scaffold-mediated osteogenesis and angiogenesis. Mater Sci Eng C Mater Biol Appl 121:111868. https://doi.org/10.1016/j.msec.2021.111868
32. Yang CY, Yu YR, Wang XC et al (2021) Cellular fluidic-based vascular networks for tissue engineering. Eng Regener 2:171–174. https://doi.org/10.1016/j.engreg.2021.09.006
33. Lin ZJ, Shen DN, Zhou WX et al (2021) Regulation of extracellular bioactive cations in bone tissue microenvironment induces favorable osteoimmune conditions to accelerate in situ bone regeneration. Bioactive Mater 6(8):2315–2330. https://doi.org/10.1016/j.bioactmat.2021.01.018
34. Shahi A, Aslani S, Ataollahi M et al (2019) The role of magnesium in different inflammatory diseases. Inflammopharmacology 27(4):649–661. https://doi.org/10.1007/s10787-019-00603-7
35. Zhai ZJ, Qu XH, Li HW et al (2014) The effect of metallic magnesium degradation products on osteoclastinduced osteolysis and attenuation of NF-kB and NFATc1 signaling. Biomaterials 35(24):6299–6310. https://doi.org/10.1016/j.biomaterials.2014.04.044
36. Chen GP, Zhang H, Wang H et al (2021) Immune tolerance induced by immune-homeostatic particles. Eng Regener 2:133–136. https://doi.org/10.1016/j.engreg.2021.09.007
37. Lee BH, Shirahama H, Cho NJ et al (2015) Efficient and controllable synthesis of highly substituted gelatin methacrylamide for mechanically stiff hydrogel. RSC Adv 5(128):106094–106097. https://doi.org/10.1039/c5ra22028a
38. Chen H, Zhang YJ, Ni TY et al (2021) Construction of a silk fibroin/polyethylene glycol double network hydrogel with co-culture of huvecs and ucmscs for a functional vascular network. ACS Appl Bio Mater 4(1):406–419. https://doi.org/10.1021/acsabm.0c00353
39. Dai X, Zhang Y, Gao L et al (2015) A mechanically strong, highly stable, thermoplastic, and self-healable supramolecular polymer hydrogel. Adv Mater 27(23):3566–3571. https://doi.org/10.1002/adma.201500534
40. Wu TL, Xu ZY, Zhang YY et al (2018) A ph-responsive biodegradable high-strength hydrogel as potential gastric resident filler. Macromol Mater Eng 303(10):1800290. https://doi.org/10.1002/mame.201800290
41. Zhao X, Jiang SC, Liu S et al (2015) Optimization of intrinsic and extrinsic tendon healing through controllable water-soluble mitomycin-C release from electrospun fibers by mediating adhesion-related gene expression. Biomaterials 61:61–74. https://doi.org/10.1016/j.biomaterials.2015.05.012
42. Lima FDS, Da Rocha Romero AB, Hastreiter A et al (2018) An insight into the role of magnesium in the immunomodulatory properties of mesenchymal stem cells. J Nutr Biochem 55:200–208. https://doi.org/10.1016/j.jnutbio.2018.02.006
43. Glenske K, Donkiewicz P, Koewitsch A et al (2018) Applications of metals for bone regeneration. Int J Mol Sci 19(3):826. https://doi.org/10.3390/ijms19030826

44. Zhang L, Yang CX, Li J et al (2014) High extracellular magnesium inhibits mineralized matrix deposition and modulates intracellular calcium signaling in human bone marrow-derived mesenchymal stem cells. Biochem Biophys Res Commun 450(4):1390–1395. https://doi.org/10.1016/j.bbrc.2014.07.004
45. Xin T, Mao J, Liu L et al (2020) Programmed sustained release of recombinant human bone morphogenetic protein-2 and inorganic ion composite hydrogel as artificial periosteum. ACS Appl Mater Interfaces 12(6):6840–6851. https://doi.org/10.1021/acsami.9b18496
46. Yu YK, Wang Y, Zhang WD et al (2020) Biomimetic periosteum-bone substitute composed of preosteoblast-derived matrix and hydrogel for large segmental bone defect repair. Acta Biomater 113:317–327. https://doi.org/10.1016/j.actbio.2020.06.030
47. Xu Z, Fan C, Zhang Q et al (2021) A self-thickening and self-strengthening strategy for 3D printing high-strength and anti-swelling supramolecular polymer hydrogels as meniscus substitutes. Adv Funct Mater 31(18):2100462. https://doi.org/10.1002/adfm.202100462
48. Kawecki F, Clafshenkel WP, Fortin M et al (2018) Biomimetic tissue-engineered bone substitutes for maxillofacial and craniofacial repair: the potential of cell sheet technologies. Adv Healthc Mater 7(6):1700919. https://doi.org/10.1002/adhm.201700919
49. Zhang YB, Liu XC, Zeng LD et al (2019) Polymer fiber scaffolds for bone and cartilage tissue engineering. Adv Funct Mater 29(36):1903279. https://doi.org/10.1002/adfm.201903279
50. Ma QL, Zhao LZ, Liu RR et al (2014) Improved implant osseointegration of a nanostructured titanium surface via mediation of macrophage polarization. Biomaterials 35(37):9853–9867. https://doi.org/10.1016/j.biomaterials.2014.08.025
51. Meagher MJ, Weiss-Bilka HE, Best ME et al (2016) Acellular hydroxyapatite-collagen scaffolds support angiogenesis and osteogenic gene expression in an ectopic murine model: effects of hydroxyapatite volume fraction. J Biomed Mater Res A 104(9):2178–2188. https://doi.org/10.1002/jbm.a.35760
52. Wrobel E, Leszczynska J, Brzoska E (2016) The characteristics of human bone-derived cells (HBDCs) during osteogenesis in vitro. Cell Mol Biol Lett 21(26):8–24. https://doi.org/10.1186/s11658-016-0027-8